Large-scale earthquake sequence simulations of 3D geometrically complex faults using the boundary element method accelerated by lattice H-matrices on distributed memory computer systems

So Ozawa[1]*, Akihiro Ida[2], Tetsuya Hoshino[3], Ryosuke Ando[1]

Abstract

Large-scale earthquake sequence simulations using the boundary element method (BEM) incur extreme computational costs through multiplying a dense matrix with a slip rate vector. Recently, hierarchical matrices (H-matrices) have often been used to accelerate this multiplication. However, the complexity of the structures of the H-matrices and the communication costs between processors limit their scalability, and they therefore cannot be used efficiently in distributed memory computer systems. Lattice H-matrices have recently been proposed as a tool to improve the parallel scalability of H-matrices. In this study, we developed a method for earthquake sequence simulations applicable to 3D nonplanar faults with lattice H-matrices. We present a simulation example and verify the accuracy of our method for a 3D nonplanar thrust fault. We also performed performance and scalability analyses of our code. Our simulations, using over 10^5 degrees of freedom, demonstrated a parallel acceleration beyond 10^4 MPI processors and a >10-fold acceleration over the best performance when the normal H-matrices are used. Using this code, we can perform unprecedented large-scale earthquake sequence simulations on geometrically complex faults with supercomputers.

Keywords: Boundary element method, H-matrix, Earthquake sequence simulation, Parallel computing, Rate and state friction

1 Introduction

Earthquake sequence simulations using rate and state friction laws originate from Tse & Rice (1986) and Rice (1993). Several researchers now use earthquake sequence simulations to understand how faults behave under various conditions and how different model ingredients (e.g., fault rheology) influence an earthquake sequence (Erickson et al., 2020). Among various computational methods, the

[1] Department of Earth and Planetary Science, University of Tokyo, Tokyo, Japan
[2] Research Institute for Value-Added-Information Generation (VAiG), Japan Agency for Marine-Earth Science and Technology (JAMSTEC), Yokohama, Japan.
[3] Information Technology Center, University of Tokyo, Chiba, Japan.
* corresponding author: sozawa@eps.s.u-tokyo.ac.jp

boundary element method (BEM) is often used because of its ease in handling complex fault geometries (Hori et al., 2004; Ohtani et al., 2014; Qiu et al., 2016; Thompson & Meade, 2019; Yu et al., 2018), although different methods were also developed (e.g. Liu et al., 2020).

A major challenge in earthquake sequence simulations is their computational cost. To simulate smaller earthquakes, the size of each element must be smaller, which increases the number of elements N. In 3D simulations (2D fault in 3D space), if the characteristic element size is reduced by a factor of 2, the increase in N is a factor of 4. In the original BEM, the computational cost for each time step scales with $O(N^2)$, where N is the number of discretized elements. This is because multiplications of a dense matrix and a vector (slip rate distribution) are necessary to evaluate the stress change on each element at every time step. Furthermore, the time step width must be small if we use small elements, which increases the repetition of matrix-vector multiplications. Thus, the computational cost increases rapidly with a decrease in the element size.

Several methods have reduced the complexity of $O(N^2)$ to $O(NlogN)$. The fast Fourier transform (FTT) method is often used for this purpose (Kato, 2003; Lapusta & Liu, 2009), but is limited to planar faults due to the assumption of translational symmetry. FTT also cannot process non-vertical faults. The use of hierarchical matrices (H-matrices) (Hackbusch, 1999) is an alternative that can be used for general fault geometries. Ohtani et al. (2011) showed a significant acceleration in earthquake cycle simulations with H-matrices, and it is now common to use H-matrices in BEM-based quasi-dynamic earthquake sequence simulations (Galvez et al., 2020; Heimisson, 2020; Hyodo et al., 2016; Ohtani et al., 2014; Ozawa & Ando, 2021; Romanet, 2017). For example, Hyodo et al. (2016) performed earthquake sequence simulations in the Nankai trough megathrust using ~300,000 elements. H-matrices have also recently been used in dynamic rupture simulations (Sato & Ando, 2021).

Parallel scalability is also important in computations using supercomputers. Owing to the increase in MPI communication costs and load imbalance, the parallel speed increase is generally less than the expectation from the ideal linear scalability. Ida et al. (2014) showed that the computational speed of an H-matrix-vector multiplication saturates <100 cores in the Poisson equation of the $N\sim100{,}000$ problem. Thus, we could not efficiently use a large number of cores in the H-matrices.

As a solution to this problem, Ida (2018) proposed the lattice H-matrices. The lattice H-matrices contain convenient structures to construct an efficient communication pattern compared with the normal H-matrices while maintaining the $O(NlogN)$ memory compression. In addition, a relatively adequate load balance is maintained in the case of lattice H-matrices, even if a large number of MPI processes are used. This method reduces the load imbalance and communication cost between MPI processes and improves parallel scalability, and it has been applied to micromagnetic simulations (Ida et al., 2020).

In this paper, we present a state-of-the-art quasi-dynamic earthquake simulator using conventional and lattice H-matrices, which is applicable to arbitrarily shaped fault(s) embedded in half-space. In Section 2, we describe the method for BEM-based earthquake sequence simulations. In Section 3, normal and lattice H-matrices are described. In Section 4, we show the simulation results for a nonplanar thrust fault. In Section 5, we measure the performance and parallel scalability. Section 6 discusses and concludes the study.

2 Method of Earthquake Sequence Simulations on 3D nonplanar faults

2.1 Boundary Element Method

In BEM, the shear stress change $\Delta\tau$ and normal stress change $\Delta\sigma$ are represented as the integral of the kernel function multiplied by the slip distribution on the fault surface:

$$\Delta\tau(\boldsymbol{x}) = \int K_{shear}(\boldsymbol{x},\boldsymbol{\xi})\Delta u(\boldsymbol{\xi})dS(\boldsymbol{\xi}), \quad (1)$$

$$\Delta\sigma(\boldsymbol{x}) = \int K_{normal}(\boldsymbol{x},\boldsymbol{y})\Delta u(\boldsymbol{\xi})dS(\boldsymbol{\xi}), \quad (2)$$

where K_{shear} and K_{normal} are elastostatic Green's functions, and Δu is the slip distribution.

To numerically calculate equations (1-2), we divide the fault surface into N elements and denoted the index set as $I = \{1, \dots, N\}$. The shapes of the elements are either rectangular or triangular. In a discretized form using step functions as the base functions, the stress changes on the i-th element are represented as:

$$\Delta\tau_i = \sum_j^N A_{ij} D_j\,, \quad (3)$$

$$\Delta\sigma_i = \sum_j^N B_{ij} D_j\,. \quad (4)$$

where $D \in \mathbb{R}^N$, A, and B $\in \mathbb{R}^{N\times N}$ are dense matrices. The entries of A and B are calculated using the techniques of Nikkhoo & Walter (2015) and Okada (1992) for uniform slip (i.e., piecewise-constant interpolation) in triangular and rectangular elements, respectively. The evaluation point of the stress component is the center of each element.

Triangular unstructured elements have more flexibility in fault geometry than rectangular elements. However, for purely vertical faults, triangular meshes using the Nikkhoo & Walter (2015) code often fail to calculate the correct entry of A and B when a large number of elements are used due to rounding error. Additionally, Barall & Tullis (2016) found that rectangles outperform triangles in terms of the accuracy of the stress value. Therefore, rectangular elements should be used as much as possible.

Notably, the normal stress change has often been neglected in several previous earthquake sequence simulations, unlike in single-event dynamic rupture simulations. Normal stress changes originate from broken symmetries such as nonplanar faults, free surfaces, and material heterogeneities. We will show the effects of normal stress changes on the earthquake cycle in a later section.

2.2 Governing Equations

The boundary condition of each element is governed by the regularized rate and state friction law. Following Rice et al., (2001), the shear and normal tractions at each element are related as follows:

$$\frac{\tau_i}{\sigma_i} = a\text{arcsinh}\left(\frac{V_i}{2V_0}e^{-\phi_i}\right), \tag{5}$$

where $V_i(t) = \frac{dD_i}{dt}$ is the slip rate, $\phi_i(t)$ is the state variable, a is the coefficient of the direct effect, and V_0 is the reference slip rate.

The evolution law for the state variable is given by the aging law (Dieterich, 1979; Ruina, 1983):

$$\frac{d\phi_i}{dt} = \frac{b}{d_c}\left[V_0 \exp\left(\frac{f_0 - \phi_i}{b}\right) - V_i\right], \tag{6}$$

where f_0 is the reference friction coefficient, b is the coefficient of the evolution effect, and d_c is the characteristic slip distance. Using the stiffness matrix calculated in the previous section, the shear and normal stress changes are given as follows:

$$\frac{d\tau_i}{dt} = \sum_j^N A_{ij}V_j + \dot{\tau}_i - \frac{\mu}{2C_s}\frac{dV_i}{dt}, \tag{7}$$

$$\frac{d\sigma_i}{dt} = \sum_j^N B_{ij}V_j + \dot{\sigma}_i, \tag{8}$$

where μ is the rigidity, c_s is the S wave speed, $\dot{\tau}_i$ and $\dot{\sigma}_i$ are the tectonic loading rates for shear and normal stresses on the i-th element, respectively. The first terms in both equations (7-8) represent the stress rates caused by slip (time derivative of equations (3-4)). The third term for the shear stress is radiation damping, which is an approximation of inertia (Rice, 1993). Earthquake sequence simulations using this approximation are "quasi-dynamic," and the effect of this approximation has been explored in previous studies (e.g. Lapusta & Liu, 2009).

We eliminate dV_i/dt from equation (7) using the total derivative of V:

$$\frac{dV_i}{dt} = \frac{\partial V_i}{\partial \tau_i}\frac{d\tau_i}{dt} + \frac{\partial V_i}{\partial \sigma_i}\frac{d\sigma_i}{dt} + \frac{\partial V_i}{\partial \phi_i}\frac{d\phi_i}{dt}, \tag{9}$$

so that:

$$\frac{d\tau_i}{dt} = \left(1 + \frac{\mu}{2c_s}\frac{\partial V_i}{\partial \tau_i}\right)^{-1}\left[\sum_j^N S_{ij}V_j + \dot{\tau}_i - \frac{\mu}{2c_s}\left(\frac{\partial V_i}{\partial \sigma_i}\frac{d\sigma_i}{dt_i} + \frac{\partial V_i}{\partial \phi_i}\frac{d\phi_i}{dt}\right)\right], \tag{10}$$

where the partial derivatives are (from equation (5)):

$$\frac{dV_i}{d\tau_i} = \frac{2V_0}{a\sigma_i} e^{-\phi_i} \cosh\left(\frac{\tau_i}{a\sigma_i}\right), \tag{11A}$$

$$\frac{dV_i}{d\sigma_i} = -\frac{2V_0\tau_i}{a\sigma_i^2} e^{-\phi_i} \cosh\left(\frac{\tau_i}{a\sigma_i}\right), \tag{11B}$$

$$\frac{dV_i}{d\phi_i} = -\frac{2V_0}{a} e^{-\phi_i} \sinh\left(\frac{\tau_i}{a\sigma_i}\right). \tag{11C}$$

2.3 Time Integration scheme

Based on equations (6), (8), and (10), we solve a $3N$ set of ordinary differential equations (ODEs) $\frac{d\boldsymbol{y}}{dt} = f(\boldsymbol{y})$ where $\boldsymbol{y} = (\phi_1, \dots, \phi_N, \tau_1, \dots \tau_N, \sigma_1, \dots, \sigma_N)$ using the Runge-Kutta method with adaptive time-stepping (Press et al., 2007). We compute $y(t + \Delta t)$ with 5th order accuracy. See Figure 1 for details.

If the maximum value of the relative difference between the 4th and 5th solution is larger than the allowance ε_{RK}, we retry the time integration as follows:

$$\Delta t_{new} = \max\left(\frac{\Delta t_{try}}{2}, \quad 0.9\Delta t_{try}{\varepsilon_{RK}}^{-0.25}\right) \tag{12}$$

If the error is below the threshold, we update the variables and calculate the next time step using the following formula:

$$\Delta t_{new} = \min\left(2\Delta t_{try}, \quad 0.9\Delta t_{try}{\varepsilon_{RK}}^{-0.2}\right). \tag{13}$$

As a result, the time step is approximately inversely proportional to the maximum slip rate. This property results from the displacement in each time step having to be smaller than the characteristic state evolution distance. Lapusta et al., (2000) and many other studies explicitly adapted inverse-slip rate time-step widths based on stability analyses. The resultant Δt weakly decreases with decreasing the element size if other parameters are identical.

The slip is thus updated as follows:

$$D_i(t + \Delta t) = D_i(t) + \frac{\Delta t}{2}\left(V_i(t) + V_i(t + \Delta t)\right). \tag{14}$$

```
Step1: compute ytemp using dt (rkck)
compute dydx(y0)
y1=y0+dt*B21*dydx(y0)
compute dydx(y1)
y2=y0+dt*(B31*dydx(y0)+B32*dydx(y1))
compute dydx(y2)
y3=y0+dt*(B41*dydx(y0)+B42*dydx(y1)+B43*dydx(y2))
compute dydx(y3)
y4=y0+dt*(B51*dydx(y0)+B52*dydx(y1)+ B53*dydx(y2)+B54*dydx(y3))
compute dydx(y4)
y5=y0+dt*(B61*dydx(y0)+B62*dydx(y1)+ B63*dydx(y2)+B64*dydx(y3)+B65*dydx(y4))
compute dydx(y5)
ytemp=y0+dt*(C1*dydx(y0)+C3*dydx(y2)+ C4*dydx(y3)+C6*dydx(y5))
yerr= dt*(D1*dydx(y0)+D3*dydx(y2)+ D4*dydx(y3)+D5*dydx(y4)+D6*dydx(y5))

Step2: control the error (rkqs)
compute the error for each process
MPI communication to compute the maximum error
If max error>allowance:
  go back to step1 using decreased step width
else:
  y=ytemp
  t=t+dt
  determine the next step width dt
```

Figure 1: Algorithm of the Runge-Kutta method with an adaptive step size (Press et al. 2007). The function dydx, which appears six times, includes two matrix-vector multiplications (equations (7) and (8)).

3 H-matrices

The most time-consuming step in solving the ODEs is the matrix-vector multiplication in equations (7-8) because it has an $O(N^2)$ complexity, whereas others display an $O(N)$ complexity (hereafter referred to as the $O(N)$ part). To advance the one-time integration, we perform six matrix-vector multiplications for shear and normal stress rates (Figure 1). We aim to reduce the complexity to $O(NlogN)$ using H-matrices.

3.1 H-matrices

H-matrices are an efficient method to compress the memory of the dense matrix derived from the integral operator (Borm et al., 2006; Hackbusch, 1999). The 3D elastostatic kernel exhibits $|\boldsymbol{x}-\boldsymbol{\xi}|^{-3}$ decay, and this kernel function can locally degenerate for a distant source and receiver points ($K(\boldsymbol{x},\boldsymbol{\xi}) \sim \sum_k g_k(\boldsymbol{x}) h_k(\boldsymbol{\xi})$). This allows for constructing H-matrices for dense matrices A and B in equations (3-4) for typical mesh geometries.

3.1.1 Construction of H-matrix

The construction of a H-matrix consists of the following steps (Borm et al., 2006). First, we construct a binary cluster tree for the set of triangular or rectangular elements using the (x, y, z) coordinates of their centers. We denote a cluster set as Ω_i $(i = 1, \dots, N_\Omega)$. We set the minimum cluster size to 15. Then, we construct a partition structure of the matrix using the following admissibility condition:

$$min\left(diam(\Omega_i), diam\left(\Omega_j\right)\right) < \eta\, dist(\Omega_i, \Omega_j) \tag{15}$$

where *diam* is the diameter of the cluster and *dist* is the distance between the two clusters. This condition is derived from the ability of the kernel function to approximately degenerate for distant source and receiver points. Typically, we set the parameter $\eta = 2$.

Figure 2 shows the partition structure of a square-shaped fault plane divided by triangular meshes. We reorder the index of the elements $I = (1, \dots, N)$ according to the structure of the cluster tree in the construction of the matrix structure. Blocks located at far-diagonal parts tend to be larger than those around diagonal parts because they correspond to the interactions of distant locations, and the admissibility condition is easy to satisfy (see equation (15)).

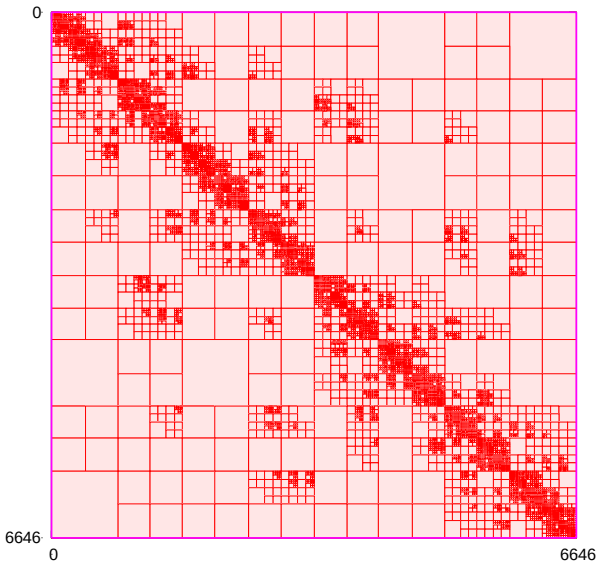

Figure 2: Block structures of H matrices (A square-shaped fault using 6646 triangular elements) made by the admissibility condition $\eta = 2$.

Let $L, M \subset I$, and $A_{LM} \in \mathbb{R}^{L\times M}$ be a submatrix of $A \in \mathbb{R}^{N\times N}$. A submatrix A_{LM} is compressed by a low-rank approximation if possible; otherwise, we use the dense matrix (full-rank matrix). A low-rank approximated submatrix A_{LM} is represented as follows:

$$A_{ij} \approx \tilde{A}_{ij} = \sum_{k=1}^{r_{LM}} g_{ki} h_{kj}\,, \tag{16}$$

where $g \in \mathbb{R}^{L\times r}, h \in \mathbb{R}^{r\times M}$, and r_{LM} is the rank of the approximated matrix. We apply the adaptive cross approximation(ACA) (Bebendorf, 2000) as the LRA. The rank r_{LM} is controlled by the error tolerance, ε_{ACA};

$$\frac{\left\|A - \tilde{A}\right\|_F}{\|A\|_F} < \varepsilon_{ACA}, \tag{17}$$

where F denotes the Frobenius norm. We use the method proposed by Ida et al. (2015) to prevent the H-matrix from having an excessively large rank.

3.1.2 H-matrix and vector multiplication (HMVM)

A matrix-vector multiplication AV is performed submatrix-wise as follows:

$$\sum_{j}^{|L|} A_{ij} V_j \approx \sum_{j}^{|L|}\sum_{k}^{r_{LM}} g_{ki} h_{kj} V_j = \sum_{k}^{r_{LM}} g_{ki} \left(\sum_{j}^{|L|} h_{kj} V_j \right). \tag{18}$$

The original computation using dense matrices requires $O(|L|\,|M|)$, while it becomes $O((|L|+|M|)r_{LM})$ in H matrix-vector multiplication (HMVM). If the rank r_{LM} is much smaller than $min(|L|,|M|)$, the number of operations is significantly reduced. The computation of equation (18) results in a part of the vector, and the full vector is obtained by taking the summation of all the submatrix-wise HMVMs.

3.1.3 Parallel Earthquake Sequence Simulation using H-matrices

Our earthquake sequence simulation code is parallelized using a message passing interface (MPI). Submatrices on the H-matrix are assigned to MPI processes, and each MPI process contains a quasi-1D-sliced portion of the entire matrix (Figure 3a). This does not represent a complete 1D slice because a submatrix cannot be separated into multiple MPI processes. For the HMVM, each processor possesses a full slip rate vector, but the resultant stress rate vector comprises a part of the slip rate vector in general. To obtain the full stress-rate vector, each MPI process calls MPI_iSEND and MPI_iRECV by $N_p - 1$ times, where N_p denotes the number of MPI processes. The complexity of the communication cost is $O(NN_p)$. The assignment algorithm is described in detail in Ida et al. (2014).

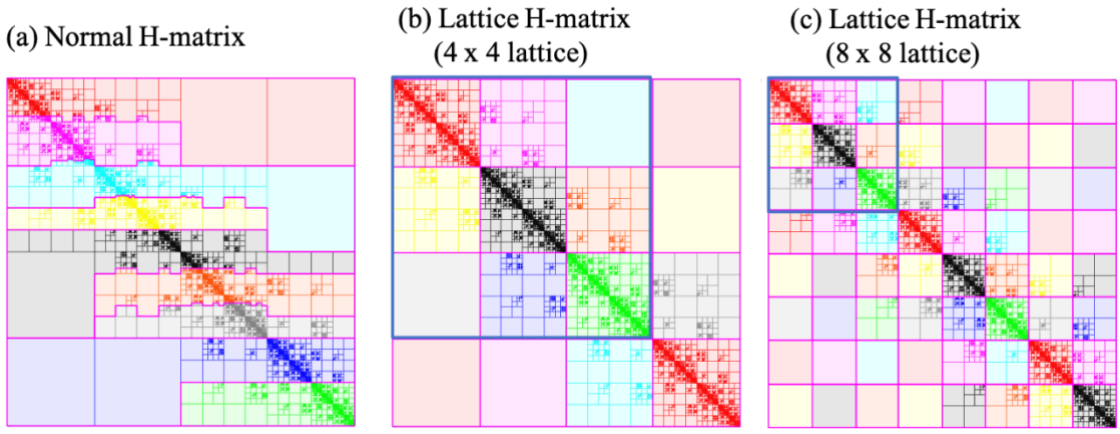

Figure 3: Comparison of the block structure and assignments to MPI processes of normal and lattice H matrices. Colors correspond to MPI processes $(N_p = 9)$. (a) is a normal H-matrix. (b) and (c) represent lattice H-matrices using 3 x 3 process grid (shown in blue frames). (b) is a 4 x 4 lattice ($q = 1$) and (c) is an 8 x 8 lattice ($q = 2$).

For $O(N)$ part (element-wise computation), each MPI process is responsible for part of the vector. To construct the full-size vector required for the HMVM, MPI_Allgather is called before the HMVM. To

perform a parallel computation of the $O(N)$ part, MPI_Scatter is called after the HMVM. As the number of MPI processes increases, the performance deteriorates owing to the MPI communication costs (both inside and outside the HMVM) in this method.

3.2 Lattice H-matrices

As previously explained, earthquake sequence simulations using H-matrices are not suitable for large-scale parallel computations because of the communication cost and load imbalance resulting from their extremely complex structure. To overcome this difficulty, Ida (2018) proposed lattice H-matrices. In this section, we describe the method for earthquake sequence simulations using lattice H-matrices. Hereafter, the H-matrices described in the previous section are referred to as normal H-matrices.

We first construct a cluster tree similar to the normal H-matrices, except for the truncation of the depth L of the cluster tree. We then construct a lattice structure using a truncated cluster tree. Then, an H-matrix is constructed for each lattice block in the same way as the normal H-matrices if it is admissible in terms of equation (15). The depth L determines the number of lattice blocks (Figure 3b and 3c).

We utilize the lattice structure for assigning MPI processes. This is achieved by introducing a process grid that has N_{pr} rows and N_{pl} columns ($N_{pr} \times N_{pl} = N_p$). We 2D-cyclically array this process grid on the lattice blocks, which means that each MPI process has discontinuous blocks of the matrix (Figure 3b and 3c). The number of lattice blocks is determined by the number of MPI processes, which ensures that q process grids are repeated in rows and columns (Figure 3b and 3c). This condition gives $L = \left\lfloor \log_2(\sqrt{N_p}q) \right\rfloor$ because the binary tree is adopted. In a fixed q, as N_p increases, each lattice becomes smaller. Thus, the entire matrix is divided into a larger number of submatrices, and the memory becomes larger compared with the normal H-matrices. However, in the procedure of HMVM using lattice H-matrices, we significantly reduce the communication traffic compared with the algorithm used in normal H-matrices. After the arithmetic of HMVM (equation (18)) assigned to each MPI process, diagonal MPI processes obtain part of the stress rate vector using MPI_Reduce along each row in the process grid, and then send it to other MPI processes in each column in the process grid using MPI_Broadcast. This algorithm, which was first proposed by Ida et al. (2018) for block low-rank matrices, utilizes the lattice structure, and to perform this algorithm, the number of processors must be a squared number (Figure 4). The complexity of the communication costs for the

HMVM using lattice H-matrices is $O(N)$ regardless of the number of MPI processes, which is reduced from that of normal H-matrices $O(NN_p)$.

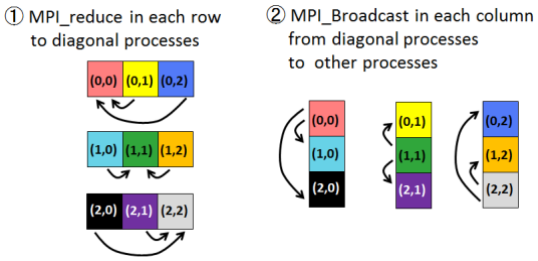

Figure 4: Schematic illustration of the algorithm of the MPI communication for HMVM (From Ida, 2018).

The HMVM in the lattice H-matrices requires only a part of the slip rate vector (size ~ $N/\sqrt{N_p}$) for each MPI process. In addition, each MPI process has identical indices of the resultant stress rate vector to the slip rate vector. Furthermore, each MPI process is in charge of the same part of the vector for element-wise computation as the HMVM. Therefore, unlike the normal H-matrix algorithm, MPI communication is not necessary before and after the HMVM. Note that this algorithm performs redundant computations for the element-wise part between $\sqrt{N_p}$ MPI processes. However, HMVM comprises ~90% of the computational time in the case of $O(10^5)$ problems and a few tens of thousands of MPI processes, thus this redundant computation does not deteriorate the overall performance.

In the implementation, we use the open-source library HACApK for the construction of H-matrices and HMVM. We validated our code with normal H-matrices using a benchmark problem of a 3D vertical strike-slip fault as defined by the Simulation of Earthquakes and Aseismic Slip (SEAS) project (Erickson et al. 2020).

4 Simulation Examples

In this section, we detail a representative earthquake sequence simulation using lattice H-matrices to demonstrate its application capability and error control.

4.1 Problem setting

A nonplanar fault is embedded in an elastic half-space, with elastic constants of $c_s = 3.464$ km/s, $c_p = 6$ km/s, and $\mu = 32.04$ GPa. The fault geometry is shown in Figure 5. The fault is 50 km in the along-strike length and 20 km in the along-dip length. The shallower (30 °dip angle) and deeper (10 °dip angle) parts are smoothly connected. The fault cut the free surface. The mesh is rectangular and 256,000 elements are used. We fix $b = 0.020$ and vary the *a*-*b* values, as shown in Figure 5 in color. We set $a/b = 0.75$ in the velocity-weakening zone. The characteristic slip distance d_c is uniformly set to 0.02 m. The initial normal and shear tractions are uniformly set to 58 MPa and 100 MPa, respectively. For simplicity, we neglect the depth dependence of the initial shear and normal stresses.

To ensure numerical convergence, the following length scale of the breakdown zone has to be resolved by at least a few elements (e.g. Rubin & Ampuero, 2005)

$$L_b = \frac{\mu d_c}{b\sigma}.$$

We set $L_b \sim 5\Delta s$ for the initial (uniform) normal stress. Note that $L_b/\Delta s$ changes with time because of the change in normal stresses. The loading approach is the backslip method with a plate rate V_{pl} for both the shear and normal stresses (Heimisson, 2020).

$$\dot{\tau}_i = -V_{pl} \sum_j^N S_{ij},$$

$$\dot{\sigma}_i = -V_{pl} \sum_j^N N_{ij},$$

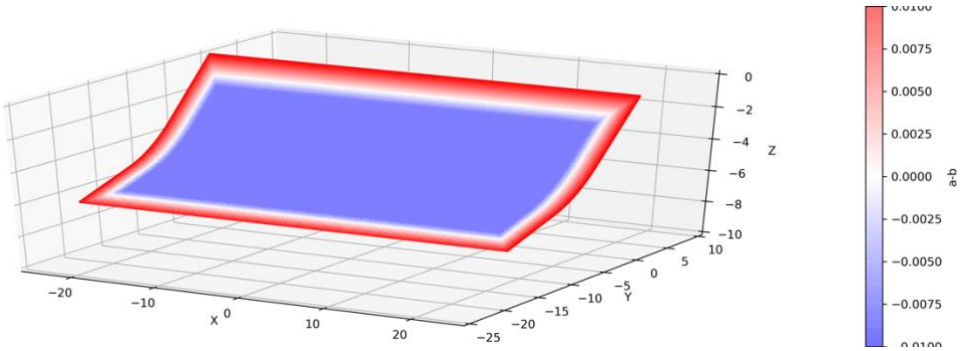

Figure 5: Fault geometry used in this study. The fault is 50 km in the along-strike length and 20 km in the along-dip length. There is a bend at dip = 10 km. The dip angle is 30 degree at the surface and 10 degree at the bottom. The color indicates the distribution of *a-b* values.

4.2 Numerical Results

Figure 6 shows the temporal variation of the cumulative slip distribution on the fault. The earthquake sequence is complex, and partial ruptures and full ruptures occur on the fault. A previous study with a 2D planar fault demonstrated that, in this type of loading, the condition of the occurrence of the partial rupture is $W/h^* \gg 1$, where W is the dimension of the velocity-weakening region and $h^*$is given by $h^* = \frac{2\mu d_c}{\pi(b-a)\sigma}$. Otherwise, only full system size ruptures occur. We assume W/h^*>10 (h *~2 km and W >20 km), and the condition of partial ruptures is met. We believe that free surface effects and fault bends would also contribute to the complex earthquake sequence by modulating the stress interaction. The purpose of this study is to examine the numerical accuracy, and a detailed discussion on the mechanism is beyond the scope of this study.

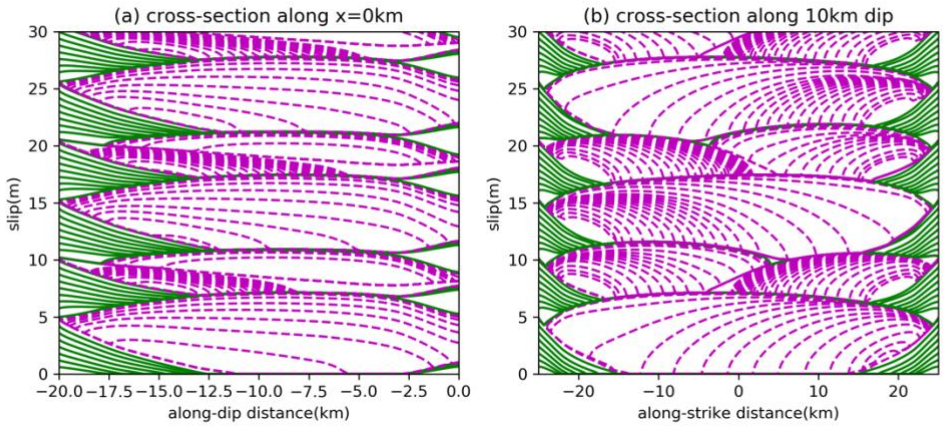

Figure 6.Cumulative slip at every 20 years during the interseismic period (green solid lines) and every 5 seconds during the coseismic period (purple dashed lines). (a) cross-section along $x = 0$ km. (b) cross-section along 10 km dip.

4.3 Case without normal stress effect

Most earthquake sequence simulations on nonplanar/dip-slip faults neglect the effect of normal stress changes (Ohtani et al. 2014, Galvez et al., 2020; Ong et al., 2019). In addition, we ran a simulation without normal stress changes (Figure 7) as a comparison. The observed differences between Figures 6 and 7 originate from the two sources of normal stress changes. First, the free surface effect leads to a coseismic normal stress reduction in the shallower part (e.g. Oglesby et al., 2000). Second, the fault curvature leads to a normal stress change that is proportional to the slip (Romanet et al., 2020). However, the coupling between the normal stress and state evolution (Tal et al., 2020), which we neglected, could partly reduce the effect of the normal stress changes.

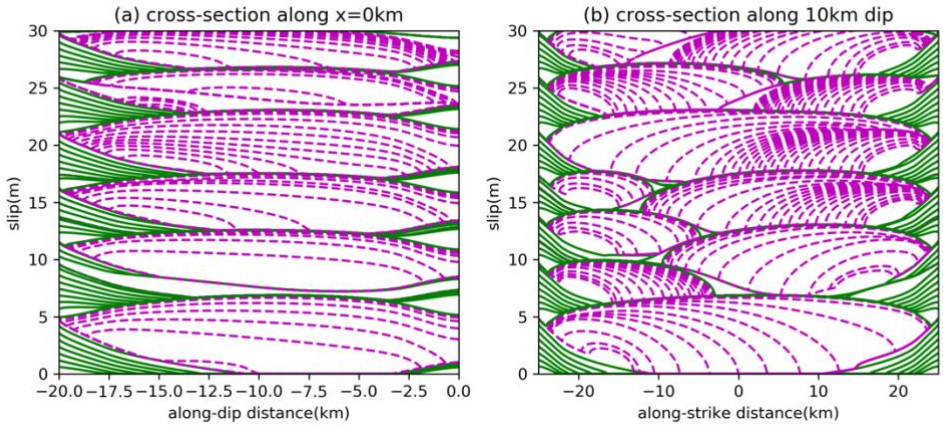

Figure 7: Same figure as Figure 6 but without considering the normal stress changes.

4.4 Effect of accuracy controls

The accuracy of the simulation is controlled by two errors: the low-rank approximation of the H-matrices and the truncation of high-order terms of the Runge-Kutta method. In this section, we explore the effect of error tolerance on the above simulation results with the normal stress change.

Figure 8a shows the results using different error tolerances of the H-matrices. We determine that $\varepsilon_{ACA} = 10^{-4}$ and 10^{-5} show no differences. $\varepsilon_{ACA} = 10^{-3}$ also matches closely with the others in terms of the timing of the event marked by spikes, although a slight difference in the nucleation phase (slow rise before the peak) for the 5th event is identified. In a simulation with $\varepsilon_{ACA} = 10^{-3}$, Ohtani et

al. (2011) documented a larger discrepancy in the timing of the event than that observed here. We suspect that the nonuniform d_c distribution (and thus nonuniform $L_b/\Delta s$ distribution) of Ohtani's model may be the cause of this discrepancy.

We also evaluate the effect of ε_{RK} in Figure 8b. Again, $\varepsilon_{RK} = 10^{-4}$ and 10^{-5} show no visible differences. In the case of $\varepsilon_{RK} = 10^{-3}$, the timing of earthquakes does not change, but the maximum slip rate fluctuates during the interseismic period. The number of time steps for 800 years using $\varepsilon_{RK} = 10^{-3}, 10^{-4}$, and 10^{-5} are 28400, 32300, and 42400, respectively.

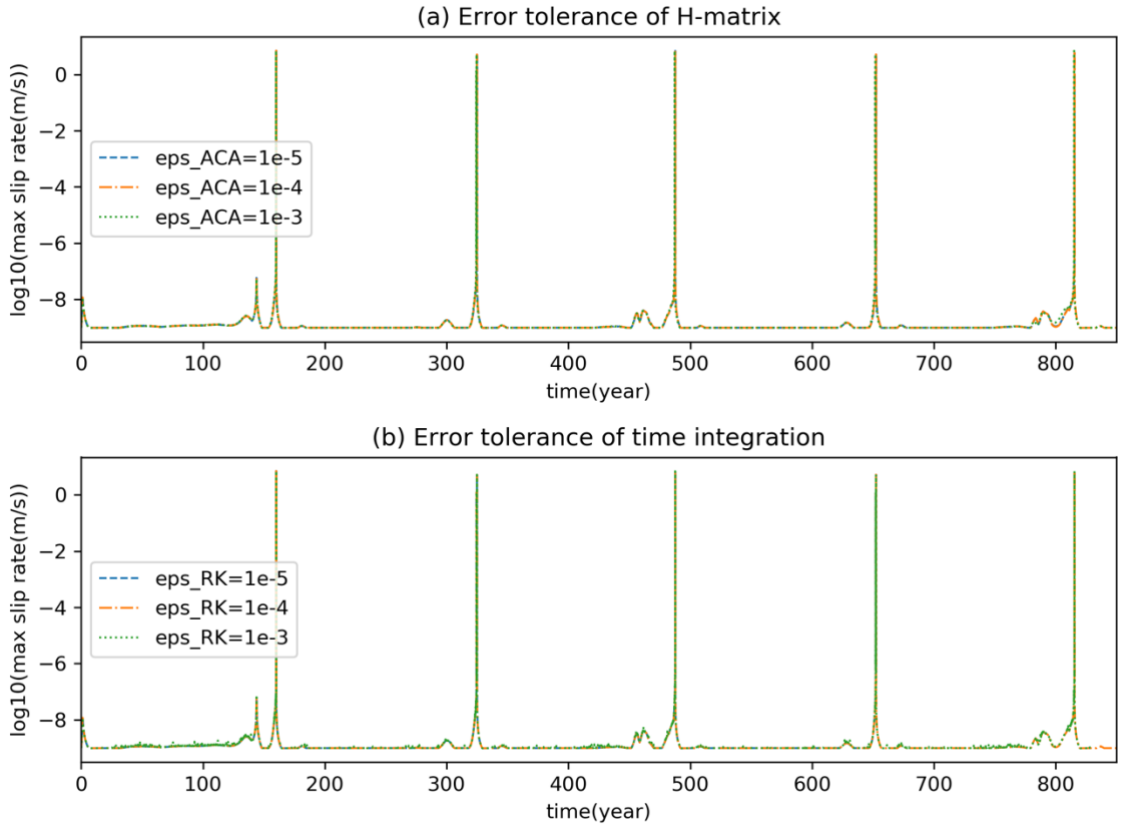

Figure 8: Maximum slip rate plotted against time. (a) Effect of the error tolerance of the ACA in constructing a lattice H-matrix and (b) effect of the error tolerance of the Runge-Kutta method.

5 Performance and scalability

In this section, we detail the performance and parallel scalability of our simulations. All simulations were performed in Oakforest-PACS(OFP) at the University of Tokyo, which is equipped with an Intel® Xeon Phi ™ 7250 (68 cores, 1.4 GHz) and 96 GB(DDR4) memory in addition to 16 GB(MCDRAM) memory. The OFP system utilizes Intel® Omni-Path for the interconnect network, which has a link throughput of 100 Gbps. We used 64 cores per CPU node. We also used an Intel Fortran compiler with the -O3 optimization option and an Intel MPI Library. All results are flat MPI parallelization. The physical problem setting is described in section 4.2.

5.1 Memory Usage of H-matrices and Lattice H-matrices

Like Ohtani et al. (2011), we investigate the compression efficiencies of the normal and lattice H-matrices. Figure 9 shows the memory size of the normal H-matrices as a function of the number of elements. We fix the fault geometry and change the element size to vary the number of elements. Figure 9a shows the case for the rectangular elements. We confirm a roughly $O(NlogN)$ dependence on the memory size for both the shear and normal stresses. For shear stresses, the compressibility against the original dense matrix is 8% for $N = 16{,}000$ and 0.7% for $N = 400{,}000$. Shear stresses have systematically larger memories than normal stresses for a given number of elements. However, the memory size also depends on the fault geometry. We also try a planar thrust fault with 30 degree dip angle (i.e. same geometry as the original except the bend) for a comparison. We find 20-30% memory reductions for normal stresses, but shear stresses have little change (Figure 9a). The matrices for nonplanar faults do not simply decay with the distance of the source and receiver around the fault bend, which increases the ranks of part of submatrices. The memory size of normal stresses is more sensitive to the fault geometry because the deviation from planar faults due to the curvature is dominant in normal stresses (Romanet et al. 2020).

We also measure the memory size of the normal H-matrices with the same geometry using triangular unstructured meshes. As shown in Figure 9b, triangular meshes have larger memories than rectangular elements. This is presumably caused by the slightly non-uniform element sizes in unstructured meshes, which lowers the efficiency of the low-rank approximation of the submatrices.

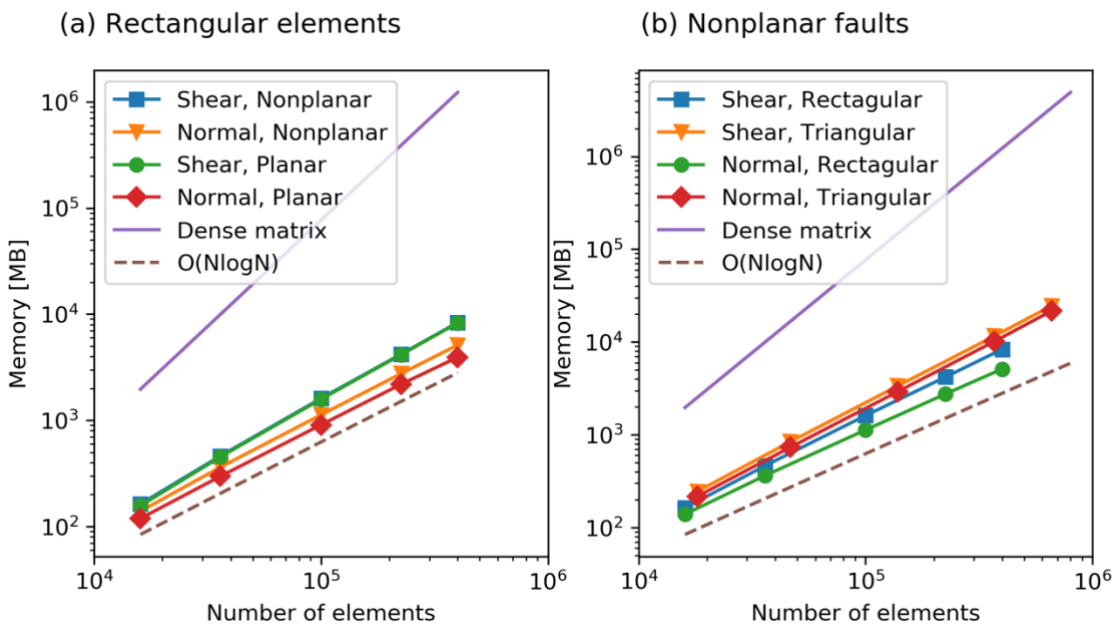

Figure 9: Memory sizes of the H matrix with respect to the number of elements. (a) Comparison of nonplanar and planar fault geometries using rectangular elements. (b) Comparison of rectangular and triangular elements using the nonplanar fault geometry. The memory size of the dense matrix ($O(N^2)$) and an $O(NlogN)$ slope are also shown as a reference.

Next, we measure the memory size of lattice H-matrices by varying the number of MPI processes (in concept, the memory size of the normal H-matrices does not depend on the number of MPI processes). We set $q = 4$ except for $N_p = 1$. As expected, the overall memory size of the lattice H-matrices increases with the number of MPI processes because of the smaller off-diagonal block sizes (Figure 10a). However, the maximum memory among the MPI processes is the bottleneck in the computation of HMVM, which is plotted in Figure 10b. For N_p<1,000, normal H-matrices are superior because the memory sizes of the diagonal MPI processes in the process grid tend to be large in lattice H-matrices. For N_p>1,000, the lattice H-matrices perform better. The saturation of the maximum memory in normal H-matrices corresponds to the submatrix that has the largest memory.

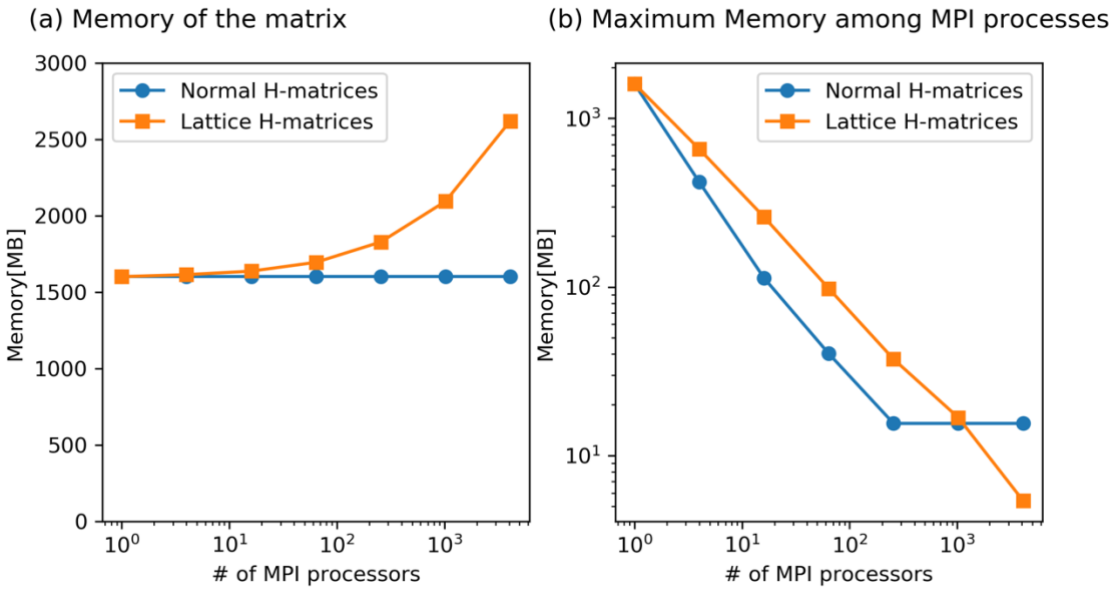

Figure 10: (a) Overall memory sizes of the normal and lattice H-matrices. (b) Maximum memory size among MPI processes. The case for shear stress and 100,000 rectangular elements.

5.2 Execution time and parallel scalability

For lattice H-matrices, we measure the dependence of the number of elements on the execution time of 100 time steps using 100 and 900 MPI processes (Figure 11). As expected, we confirm a $O(NlogN)$ or slightly steeper increase in the execution time.

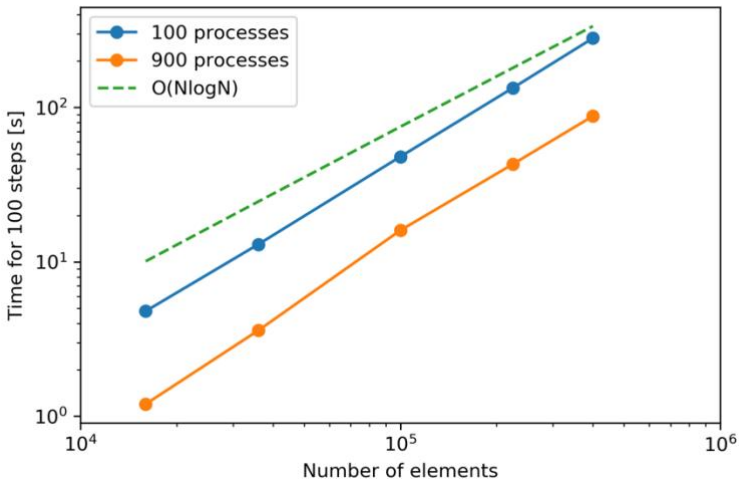

Figure 11: Number of elements vs. execution time of 100 time steps with the lattice H-matrices. $O(NlogN)$ curve is also shown as a reference.

Next, we measure parallel scalability (Figure 12). Our simulation using lattice H-matrices shows a consistent sublinear acceleration beyond 30,000 cores in the case of $N = 400{,}000$. We also show the result of the normal H-matrices, which exhibits an almost linear acceleration up to ~20 cores but rapidly saturates ~100 cores. The speed-down over 100 cores is caused by the increase in the communication cost, which is proportional to N_p.

By comparing the two methods, the normal H-matrices are faster by up to a few hundred MPI processes. The deceleration of lattice H-matrices from normal H-matrices occurred because the maximum memory for an MPI process is larger than that of normal H-matrices, as shown in the previous section (Figure 10b). The lattice H-matrices outperform normal H-matrices beyond a few 100s of cores owing to the reduction in the communication cost. We do not observe the saturation of the computation speed for lattice H-matrices, even with more than 10,000 cores. Figure 13 shows how a large fraction of the computation time is used in the HMVM in lattice H-matrices. The ratio of HMVM decreases with an increase in MPI processes, but it is always above 90%. From this figure, we expect a further acceleration in performance using additional processors.

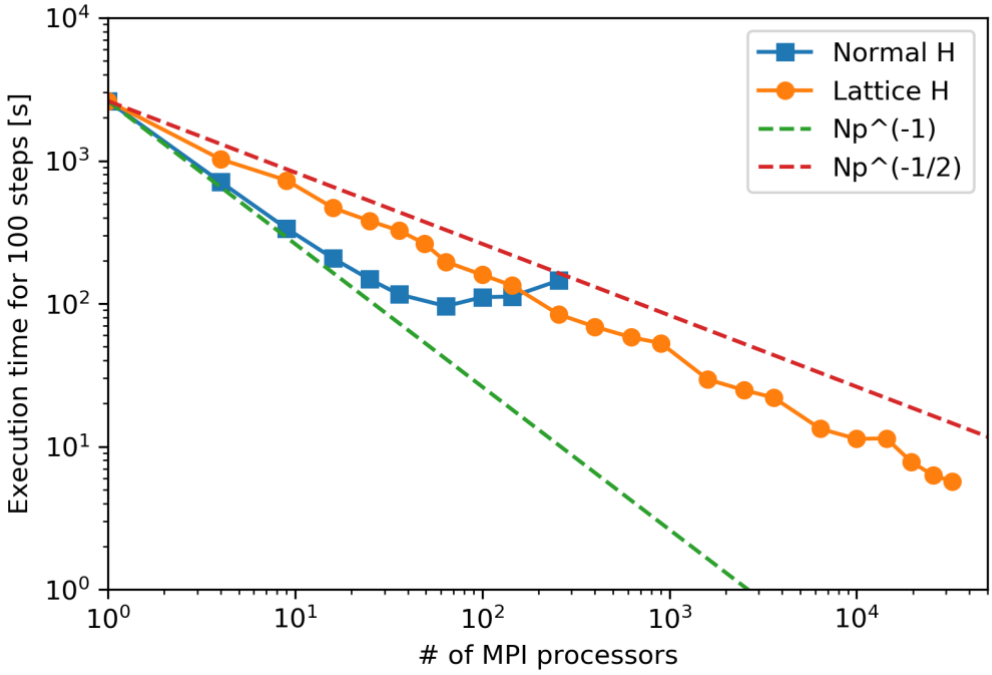

Figure 12: Parallel scalability when 100 time steps are performed (N=400,000 rectangular elements).

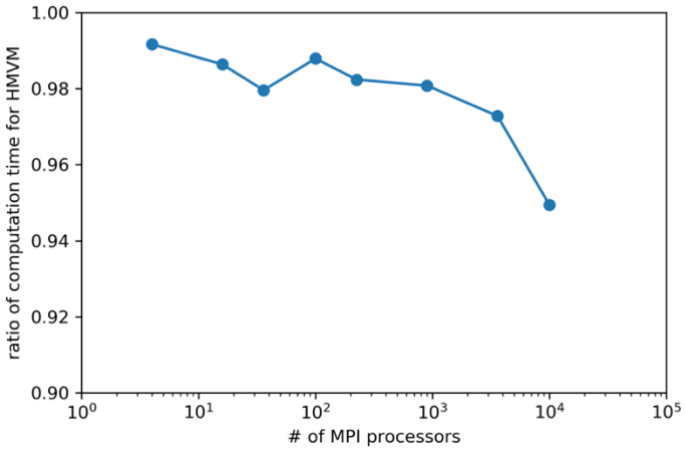

Figure 13: Ratio of calculation time of HMVM over the one time step for N=400,000.

6 Discussion and Conclusions

In this study, we developed a method for earthquake sequence simulations with BEM using normal and lattice H-matrices. This method is highly flexible with fault geometries and accounts for the normal stress evolution, which is often neglected. Numerical experiments were conducted in a 3D nonplanar thrust fault to demonstrate the accuracy of our method in terms of convergence with decreasing error tolerances in both the low-rank approximation in H-matrices and the Runge-Kutta method. Our numerical simulation using a curved thrust fault showed complex patterns in earthquake sequences, which motivates us to conduct further studies focusing on earthquake science. Our code can also be applied to natural fault systems worldwide and is potentially highly useful in physics-based earthquake hazard analyses.

In our numerical experiments, we confirmed $O(NlogN)$ complexity for the execution time for lattice H-matrices. Although Ohtani et al. (2011) also showed $O(NlogN)$ complexity, our curved fault geometry is more complex than the planar thrust fault model used by them. One question is that whether this $O(NlogN)$ complexity is maintained for further complex geometries, such as rough faults and/or fault networks (Ozawa & Ando, 2021). Additionally, inhomogeneous meshes can be used if the required resolution is not uniform due to spatial variation in friction and stress conditions. The use of inhomogenous meshes might change the compressibility of the dense matrices, even for planar faults. Further studies are necessary to answer these questions.

We evaluated the parallel scalability of our simulation code using a supercomputer Oakforest-PACS. The lattice H-matrices overcame the high communication costs between MPI processes and enabled efficient computation using a large number of cores. The maximum computation speed for the lattice H-matrices was greater than ten times faster than that of the normal H-matrices. However, the lattice H-matrices were not as efficient as the normal H-matrices for a small number of cores. Thus, normal H-matrices should be used when a small number of CPUs is available.

Although we only performed flat-MPI simulations, we expect further acceleration using openMP and MPI hybrid parallelization. Hybrid parallelization is especially important for extremely large (N>1,000,000) problems, as only few MPI processes can be used per CPU node because of memory limitations that cannot be distributed, such as the information of the coordinates.

Acknowledgements

This work is supported by JSPS [grant numbers 19J2167, 21H03447, 19K04031], the "Joint Usage/Research Center for Interdisciplinary Large-scale Information Infrastructures" and "High Performance Computing Infrastructure" in Japan (Project ID: jh210023-NAH), and MEXT under its Earthquake and Volcano Hazards Observation and Research Program.

Reference

Barall, M., & Tullis, T. E. (2016). The performance of triangular fault elements in Earthquake Simulators. *Seismological Research Letters*, *87*(1), 164–170. https://doi.org/10.1785/0220150163

Bebendorf, M. (2000). Numerische Mathematik Approximation of boundary element matrices. *Numerische Mathematik*, *86*, 565–589.

Borm, S., Grasedyck, L., & Hackbusch, W. (2006). Hierarchical Matrices. In *Hierarchical Matrices* (Lecture Note). Max-Plunk-Institut fur Mathematik.

Dieterich, J. H. (1979). Modeling of rock friction 1. Experimental results and constitutive equations. *Journal of Geophysical Research: Solid Earth*, *84*(B5), 2161–2168. https://doi.org/10.1029/JB084iB05p02161

Erickson, B. A., Jiang, J., Barall, M., Lapusta, N., Dunham, E. M., Harris, R., Abrahams, L. S., Allison, K. L., Ampuero, J.-P., Barbot, S., & others. (2020). The community code verification exercise for simulating sequences of earthquakes and aseismic slip (seas). *Seismological Research Letters*, *91*(2A), 874–890.

Galvez, P., Somerville, P., Petukhin, A., Ampuero, J. P., & Peter, D. (2020). Earthquake Cycle Modelling of Multi-segmented Faults: Dynamic Rupture and Ground Motion Simulation of the 1992 M w 7.3 Landers Earthquake. *Pure and Applied Geophysics*, *177*(5), 2163–2179. https://doi.org/10.1007/s00024-019-02228-x

HACApK. (n.d.). Retrieved October 22, 2021, from https://github.com/Post-Peta-Crest/ppOpenHPC/tree/MATH/HACApK

Hackbusch, W. (1999). A Sparse Matrix Arithmetic Based on H-Matrices. Part I: Introduction to H-Matrices. *Computing*, *62*(2), 89–108.

Heimisson, E. R. (2020). Crack to pulse transition and magnitude statistics during earthquake cycles on a self-similar rough fault. *Earth and Planetary Science Letters*, *537*. https://doi.org/10.1016/j.epsl.2020.116202

Hori, T., Kato, N., Hirahara, K., Baba, T., & Kaneda, Y. (2004). A numerical simulation of earthquake cycles along the Nankai Trough in southwest Japan: Lateral variation in frictional property due

to the slab geometry controls the nucleation position. *Earth and Planetary Science Letters*, *228*(3–4), 215–226. https://doi.org/10.1016/j.epsl.2004.09.033

Hyodo, M., Hori, T., & Kaneda, Y. (2016). A possible scenario for earlier occurrence of the next Nankai earthquake due to triggering by an earthquake at Hyuga-nada, off southwest Japan 4. Seismology. *Earth, Planets and Space*, *68*(1). https://doi.org/10.1186/s40623-016-0384-6

Ida, A. (2018). Lattice h-matrices on distributed-memory systems. *Proceedings - 2018 IEEE 32nd International Parallel and Distributed Processing Symposium, IPDPS 2018*, 389–398. https://doi.org/10.1109/IPDPS.2018.00049

Ida, A., Ataka, T., & Furuya, A. (2020). Lattice H-Matrices for Massively Parallel Micromagnetic Simulations of Current-Induced Domain Wall Motion. *IEEE Transactions on Magnetics*, *56*(4), 18–21. https://doi.org/10.1109/TMAG.2019.2959349

Ida, A., Iwashita, T., Mifune, T., & Takahashi, Y. (2014). Parallel hierarchical matrices with adaptive cross approximation on symmetric multiprocessing clusters. *Joirnal of Information Processing*, *22*, 642–650.

Ida, A., Iwashita, T., Ohtani, M., & Hirahara, K. (2015). Improvement of hierarchical matrices with adaptive cross approximation for large-scale simulation. *Journal of Information Processing*, *23*(3), 366–372.

Ida, A., Nakashima, H., & Kawai, M. (2018). Parallel hierarchical matrices with block low-rank representation on distributed memory computer systems. *ACM International Conference Proceeding Series*, 232–240. https://doi.org/10.1145/3149457.3149477

Kato, N. (2003). Repeating slip events at a circular asperity: Numerical simulation with a rate- and state- dependent friction law. *Bull. Earthq. Res. Inst.*, *78*, 151–166.

Lapusta, N., & Liu, Y. (2009). Three-dimensional boundary integral modeling of spontaneous earthquake sequences and aseismic slip. *Journal of Geophysical Research: Solid Earth*, *114*(9). https://doi.org/10.1029/2008JB005934

Lapusta, N., Rice, J. R., Ben-Zion, Y., & Zheng, G. (2000). Elastodynamic analysis for slow tectonic loading with spontaneous rupture episodes on faults with rate- and state-dependent friction. *Journal of Geophysical Research: Solid Earth*, *105*(B10), 23765–23789. https://doi.org/10.1029/2000JB900250

Liu, D., Duan, B., & Luo, B. (2020). EQsimu: A 3-D finite element dynamic earthquake simulator for multicycle dynamics of geometrically complex faults governed by rate- And state-dependent friction. *Geophysical Journal International*, *220*(1), 598–609. https://doi.org/10.1093/GJI/GGZ475

Nikkhoo, M., & Walter, T. R. (2015). Triangular dislocation: An analytical, artefact-free solution. *Geophysical Journal International*, *201*(2), 1119–1141. https://doi.org/10.1093/gji/ggv035

Oglesby, D. D., Archuleta, R. J., & Nielsen, S. B. (2000). The three-dimensional dynamics of dipping

faults. *Bulletin of the Seismological Society of America*, *90*(3), 616–628. https://doi.org/10.1785/0119990113

Ohtani, M., Hirahara, K., Hori, T., & Hyodo, M. (2014). Observed change in plate coupling close to the rupture initiation area before the occurrence of the 2011 Tohoku earthquake: Implications from an earthquake cycle model. *Geophysical Research Letters*, *41*(6), 1899–1906. https://doi.org/10.1002/2013GL058751

Ohtani, M., Hirahara, K., Takahashi, Y., Hori, T., Hyodo, M., Nakashima, H., & Iwashita, T. (2011). Fast computation of quasi-dynamic earthquake cycle simulation with Hierarchical Matrices. *Procedia Computer Science*, *4*, 1456–1465.

Okada, Y. (1992). INTERNAL DEFORMATION DUE TO SHEAR AND TENSILE FAULTS IN A HALF-SPACE. In *Bulletin of the Seismological Society of America* (Vol. 82, Issue 2). http://pubs.geoscienceworld.org/ssa/bssa/article-pdf/82/2/1018/2707430/BSSA0820021018.pdf

Ong, S. Q. M., Barbot, S., & Hubbard, J. (2019). Physics-Based Scenario of Earthquake Cycles on the Ventura Thrust System, California: The Effect of Variable Friction and Fault Geometry. *Pure and Applied Geophysics*, *176*(9), 3993–4007. https://doi.org/10.1007/s00024-019-02111-9

Ozawa, S., & Ando, R. (2021). Mainshock and Aftershock Sequence Simulation in Geometrically Complex Fault Zones. *Journal of Geophysical Research: Solid Earth*, *126*(2). https://doi.org/10.1029/2020JB020865

Press, W. H., Teukolsky, S. A., Vetterling, W. T., & Flannery, B. P. (2007). *Numerical recipes 3rd edition: The art of scientific computing*. Cambridge university press.

Qiu, Q., Hill, E. M., Barbot, S., Hubbard, J., Feng, W., Lindsey, E. O., Feng, L., Dai, K., Samsonov, S. v., & Tapponnier, P. (2016). The mechanism of partial rupture of a locked megathrust: The role of fault morphology. *Geology*, *44*(10), 875–878. https://doi.org/10.1130/G38178.1

Rice, J. R. (1993). Spatio-temporal complexity of slip on a fault. *Journal of Geophysical Research*, *98*(B6), 9885. https://doi.org/10.1029/93JB00191

Rice, J. R., Lapusta, N., & Ranjith, K. (2001). Rate and state dependent friction and the stability of sliding between elastically deformable solids. *Journal of the Mechanics and Physics of Solids*, *49*(9), 1865–1898.

Romanet, P. (2017). *Fast algorithms to model quasi-dynamic earthquake cycles in complex fault networks (PhD thesis)*.

Romanet, P., Sato, D. S. K., & Ando, R. (2020). Curvature, a mechanical link between the geometrical complexities of a fault: Application to bends, kinks and rough faults. *Geophysical Journal International*, *223*(1), 211–232. https://doi.org/10.1093/gji/ggaa308

Rubin, A. M., & Ampuero, J. P. (2005). Earthquake nucleation on (aging) rate and state faults. *Journal of Geophysical Research: Solid Earth*, *110*(11), 1–24. https://doi.org/10.1029/2005JB003686

Ruina, A. (1983). Slip instability and state variable friction laws. *Journal of Geophysical Research: Solid Earth*, *88*(B12), 10359–10370. https://doi.org/10.1029/JB088iB12p10359

Sato, D. S., & Ando, R. (2019). *Quasilinear Algorithm for Elastodynamic Boundary Integral Equation Method*. http://arxiv.org/abs/1903.02118

Tal, Y., Rubino, V., Rosakis, A. J., & Lapusta, N. (2020). lluminating the physics of dynamic friction throughlaboratory earthquakes on thrust faults. *PNAS*, *117*(35), 21095–21100. https://doi.org/10.1073/pnas.2004590117/-/DCSupplemental

Thompson, T., & Meade, B. (2019). *Earthquake cycle modeling of the Cascadia subduction zone*. https://doi.org/10.31223/OSF.IO/3VUXW

Tse, S. T., & Rice, J. R. (1986). Crustal earthquake instability in relation to the depth variation of frictional slip properties. *Journal of Geophysical Research: Solid Earth*, *91*(B9), 9452–9472.

Yu, H., Liu, Y., Yang, H., & Ning, J. (2018). Modeling earthquake sequences along the Manila subduction zone: Effects of three-dimensional fault geometry. *Tectonophysics*, *733*(August 2017), 73–84. https://doi.org/10.1016/j.tecto.2018.01.025